AXE D.2019.4.2.1 - CU ALLOY - LATE BRONZE AGE - FRANCE

Artefact name Axe D.2019.4.2.1

Authors Christian. Degrigny (HE-Arc CR, Neuchâtel, Neuchâtel, Switzerland) & Naima. Gutknecht (HE-Arc CR, Neuchâtel, Neuchâtel, Switzerland) & Valentina. Valbi (Laboratoire Métallurgie et Culture (LMC), Belfort, Franche-Comté, France)

Url /artefacts/1254/

The object

Credit HE-Arc CR, N.Gutknecht.

Fig. 1: Winged axe covered with a brown crust and blue-green corrosion products and showing areas of flaking,

Description and visual observation

Description of the artefact Elongated axe with median wings and curvature in the center. It is covered with a brown crust and blue-green corrosion products that show areas of flaking. Dimensions: L = 14.3cm; W = 3.1cm.

Type of artefact Tool

Origin Granges Feuillet, dépôt n°2, Salins-les-Bains, Franche-Comté, France

Recovering date 2012

Chronology category Late Bronze Age

chronology tpq 1350 B.C.

chronology taq 1150 B.C.

Chronology comment	
Burial conditions / environment	Soil
Artefact location	Musée de Lons-le-Saunier, Lons-le-Saunier, Franche-Comté
Owner	Musée de Lons-le-Saunier (dépôt de Salins-les-Bains)
Inv. number	D.2019.4.2.1
Recorded conservation data	N/a

Complementary information

From the time of excavation in 2012 until its entry into the museum in 2015, the object was kept in a food storage box in an uncontrolled environment. Flaking corrosion was documented when the object was collected and stored by the museum in 2015.

Study area(s)

Credit HE-Arc CR, N.Gutknecht.

Fig. 2: Axe with location of Fig.3 and sampling area (red triangle),

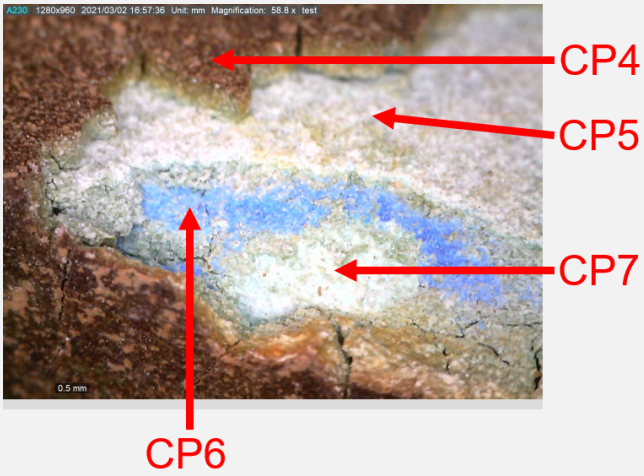

Credit HE-Arc CR, N.Gutknecht.

Fig. 3: Detail from Fig. 2 showing part of the documented strata,

Binocular observation and representation of the corrosion structure

The schematic representation below gives an overview of the corrosion structure encountered on the axe from a first visual macroscopic observation.

Strata	Type of stratum	Principal characteristics
CP1	Corrosion product	green, thin, isolated, non-compact, soft
CP2	Corrosion product	blue, thin, isolated, compact, soft

CP3	Corrosion product	black, thin, isolated, compact, soft
CP4	Corrosion product	light brown, thick, discontinuous, non-compact, soft
CP5	Corrosion product	light green, thick, discontinuous, non-compact, soft
CP6	Corrosion product	blue, thin, discontinuous, non-compact, very soft
CP7	Corrosion product	light green, medium, continuous, non-compact, soft
CP8	Corrosion product	orange, thin, isolated, non-compact, soft

Table 1: Description of the principal characteristics of the strata as observed under binocular and described according to Bertholon's method.

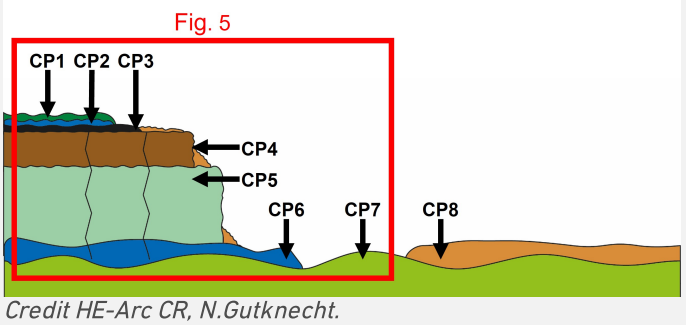

Credit HE-Arc CR, N.Gutknecht.

Fig. 4: Stratigraphic representation of the corrosion structure of the axe by macroscopic and binocular observation with indication of the corrosion structure used to build the MiCorr stratigraphy of Fig. 5 (red square),

MiCorr stratigraphy(ies) – Bi

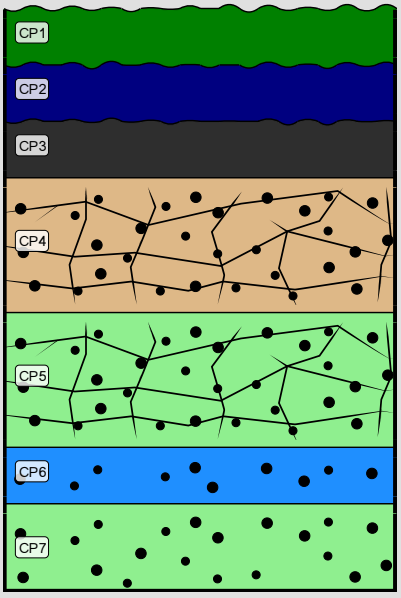

Fig. 5: Stratigraphic representation of the corrosion structure of the axe observed macroscopically under binocular microscope using the MiCorr application with reference to Fig. 4. The characteristics of the strata are only accessible by clicking on the drawing that redirects you to the search tool by stratigraphy representation, Credit HE-Arc CR, N.Gutknecht.

Sample(s)

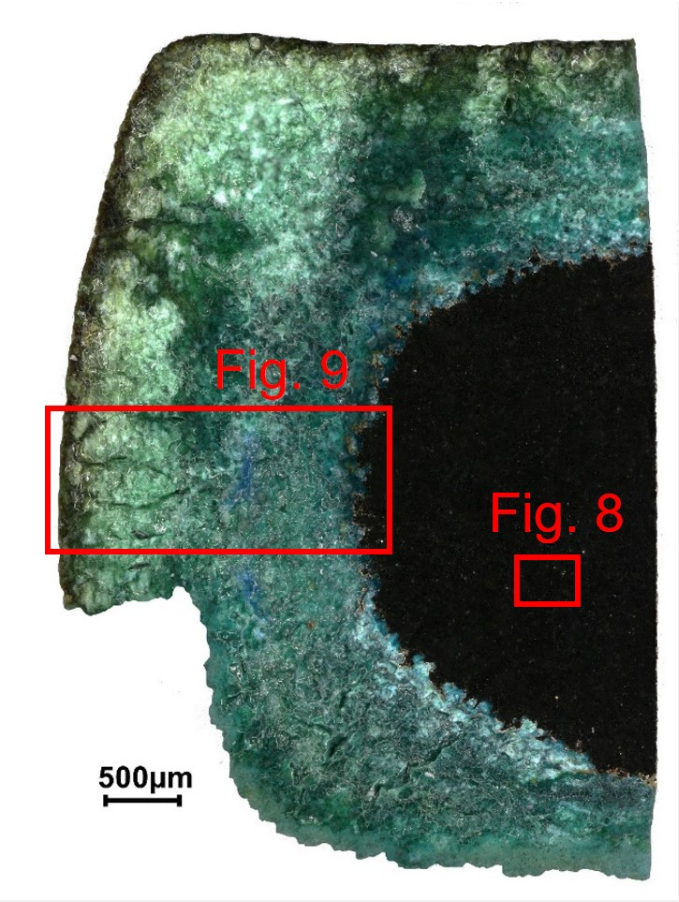

Fig. 6: Micrograph of the cross-section of the sample from Fig. 2 in dark field showing the location of Figs. 8-9,

Credit LMC-CNRS, V. Valbi.

Description of sample	The cross-section corresponds to a lateral cut (Fig. 2) and is representative of the entire thickness of the axe's body. A metallic core is present below the corrosion layers (Fig. 6).
Alloy	Cu Alloy
Technology	Annealed after cold working
Lab number of sample	
Sample location	Centre de Conservation et d'Etude René-Rémond, Lons-le-Saunier
Responsible institution	Centre de Conservation et d'Etude René-Rémond, Lons-le-Saunier
Date and aim of sampling	April 2021

Complementary information

Since the object is suffering from a flaking phenomenon of the corrosion products, a special methodology was developed in order to sample the object without loss of information. As a first step, a few drops of resin were used to "consolidate" the corrosion products and avoid their loss during the sampling. A few days later when the resin was hard, the sampling was realized with a rotatory tool and embodied in a similar resin for cross-section documentation.

Analyses and results

Analyses performed

Invasive approach (on the sample)

- Optical microscopy: the sample is polished, then it is observed with a numerical microscope KEYENCE VHX-7000 in bright and dark field.

- Metallography: the polished sample is etched with alcoholic ferric chloride and observed by optical microscopy in bright field.

- SEM-EDX: the sample is coated with a carbon layer and analyses are performed on a SEM-FEG JEOL 7001-F equipped with a silicon-drift EDX Oxford detector (Aztec analysis software) with an accelerating voltage of 20 kV and probe current at about 9 nA. The relative error is considered of about 10% for content range <1wt%, and of 2% for content range of >1wt%.

- µ-Raman spectroscopy: it is performed on a HORIBA Labram Xplora spectrometer equipped with a 532 nm laser with 1800 grating, the laser power employed is between 0.04 and 0.55 mW with acquisition time varying between 1 and 5 minutes.

- µ-X-ray Diffraction: measurements were realized using an X-Ray generator (RU-200B) in reflection mode with data collected from an angle of 5° (2θ) delivering a monochromatic beam of 600 x 30 µm at 17.5 keV (Mo, Ka1,2). Diffraction patterns were collected using a 2D detector (Pilatus 300K - Dectris). Data process was realised with PyFAI and EVA softwares using the ICDD-JCPDS database.

Non invasive analysis

None.

Metal

EDX analysis (Table 2) of the residual metal analyzed on cross-section indicates that it is a low tin bronze with 8 wt% of Sn and 1 wt% of S. The metal has a polygonal grains microstructure (Figs. 7 & 8) with several twinned grains (Fig. 8) revealing that the object underwent an annealing procedure. Sulfide Cu-S-Fe inclusions (10-50 µm, Fig. 8) and Pb inclusions (1-3 µm) are homogeneously distributed on the whole sample.

wt%	Metal (general aera)	Sulfide inclusions
Cu	90	81
Sn	8	0
S	1	18
Pb	<0.5	0
Fe	<0.5	1
Ni	<0.5	0
As	<0.5	0
Total	100	0

Table 2: Chemical composition of the alloy over a general area of analysis and of the sulfide inclusions by SEM-EDX, LMC-IRAMAT-CNRS-UTBM.

Credit LMC-CNRS, V. Valbi.

Fig. 7: Micrograph of the cross-section of the sample (same as Fig. 6) in bright field after chemical etching,

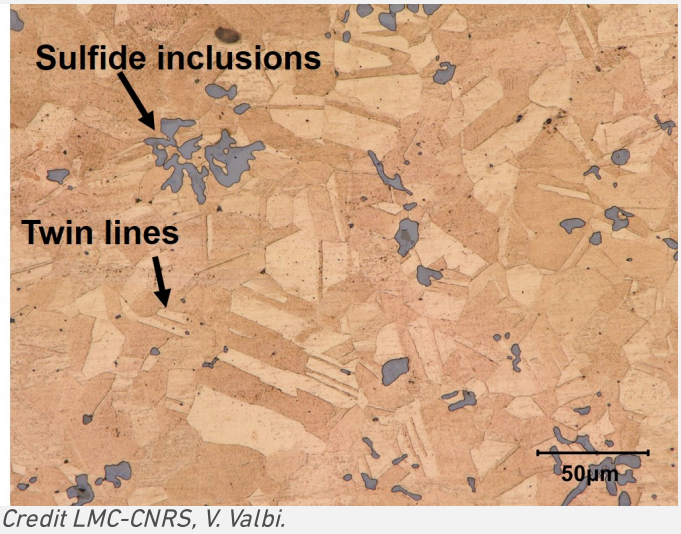

Credit LMC-CNRS, V. Valbi.

Fig. 8: Micrograph of the metal sample from Fig. 7 (detail), etched, bright field. In color, polygonal grains with twin lines and in grey sulfide inclusions,

Microstructure	Polygonal and twinned grains
First metal element	Cu
Other metal elements	S, Sn

Complementary information

None.

Corrosion layers

The observation of the sample in dark field mode shows the presence of a thick (1500-2000 µm) and porous/fractured corrosion structure. The corrosion structure can be subdivided into: a thin external olive green CP1, a light green thick CP2, a blue discontinuous CP3, a light blue CP4 with red and black inclusions, CM1 and M1 (Fig. 9).

The EDX elemental analysis (Table 3) reveals a Sn-enrichment in the whole corrosion structure (27-54 wt%) when compared to the original amount of this element in the alloy (8 wt%). The strongest Sn-enrichment is observed for CP1 and CP2, with 52-54 Sn wt%, low amounts of Cu (9-10 wt%), and a few percents of external elements such as Si and Al (1-2 wt%). CP3 is richer in Cu (around 40 Cu wt% and 27 Sn wt%), while the CP4 is richer in Sn than Cu (36 Sn wt% and 28 Cu wt%). It was also possible to analyze the black spots inside the CP4, which are composed mainly of Cu (55 wt%) and S (around 30 wt%) with 11 wt% of Ag.

XRD (Figs. 10-12) and Raman analyses (Figs. 13-16) allowed to identify different compounds of the corrosion structure. The CP2 stratum is composed of cassiterite (SnO_2). CP3 was identified as the hydroxicarbonate azurite $Cu_3(CO_3)_2(OH)_2$. CP4 is composed of mushistonite (a mixed Cu/Sn hydroxide with general formula $Cu^{2+}Sn^{4+}(OH)_6$), together with localized presence of the hydroxicarbonate malachite $Cu_2(CO_3)(OH)_2$ in the more external part close to CP3, while the red areas and the black spots inside CP4 are identified respectively as cuprite Cu_2O and (silver-bearing) covellite CuS.

wt%	CP1	CP2	CP3	CP4	CP4 black spots
Sn	53	54	27	36	1
Cu	10	9	38	28	55
O	31	31	33	34	2
Al	2	1	<0.5	0	0
Si	1	2	<0.5	0.5	<0.5
Ag	<0.5	<0.5	<0.5	<0.5	11
S	0	<0.5	<0.5	0.0	29
Pb	1	1	<0.5	<0.5	0
As	<1	<1	<0.5	<0.5	<0.5
Fe	<1	<0.5	<1	<0.5	<0.5
P	<0.5	<0.5	<0.5	<0.5	0
Cl	<0.5	<0.5	0	<0.5	0

Table 3: Chemical composition (wt%) of the corrosion layers over a general area of analysis in cross-section obtained by SEM-EDX, LMC-IRAMAT-CNRS-UTBM.

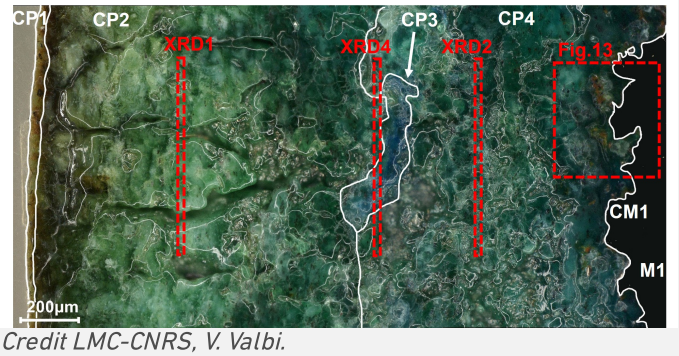

Credit LMC-CNRS, V. Valbi.

Fig. 9: Micrograph of the corrosion structure from Fig. 6 (detail), unetched, dark field with indication of the different strata of table 3 and location of XRD analyses and Fig. 13,

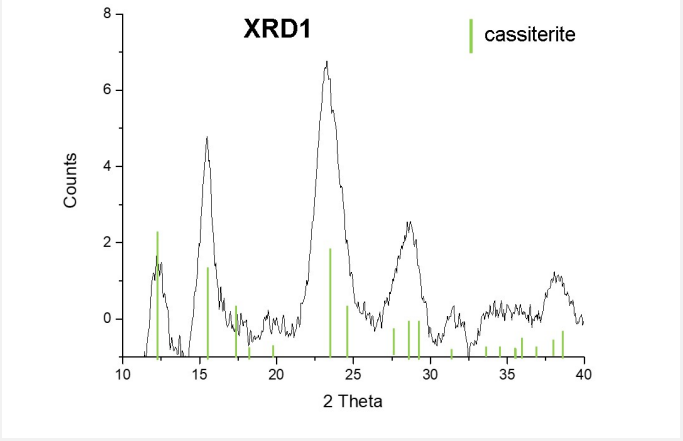

Credit LMC-CNRS, V.Valbi.

Fig. 10: XRD diffractogram 1 collected on CP2 (see location on Fig. 9),

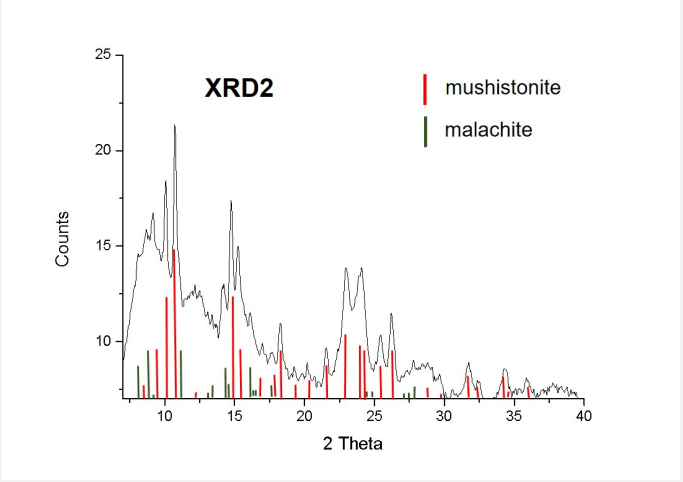

Credit LMC-CNRS, V.Valbi.

Fig. 11: XRD diffractogram 2 collected on CP4 (see location on Fig. 9),

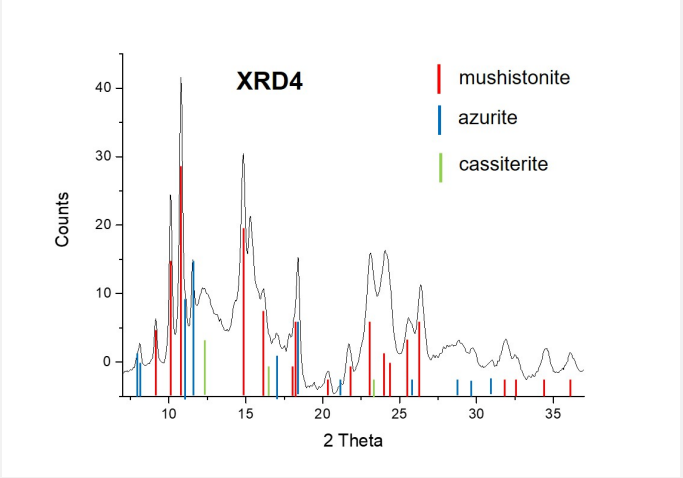

Credit LMC-CNRS, V.Valbi.

Fig. 12: XRD diffractogram 4 collected on CP3, at the interface with CP2 (see location on Fig. 9),

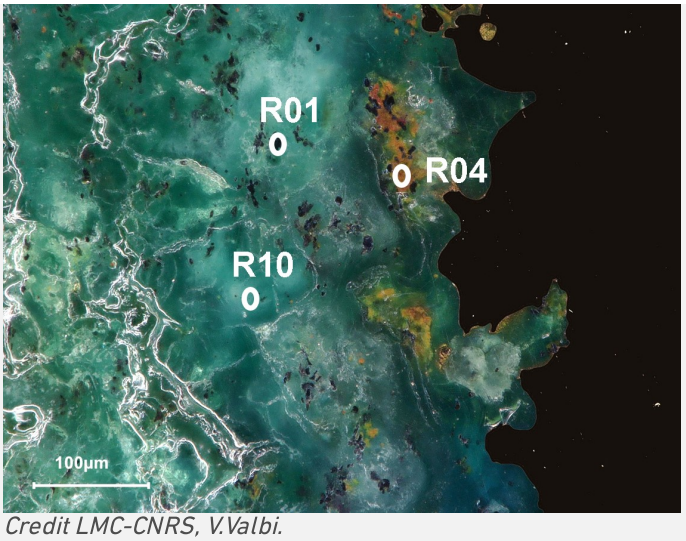

Fig.13: Micrograph of the corrosion structure, detail of CP4 from Fig.9, showing the presence of black spots of covellite and red spots of cuprite identified by Raman spectroscopy,

Credit LMC-CNRS, V.Valbi.

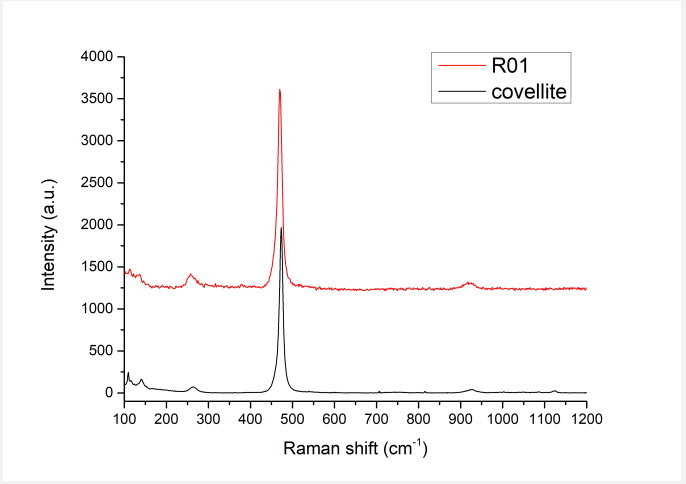

Fig. 14: Raman spectrum of point R01 performed on the black spots in CP4, as shown in Fig. 13, together with the reference for covellite RRUFFID=R060306,

Credit LMC-CNRS, V.Valbi.

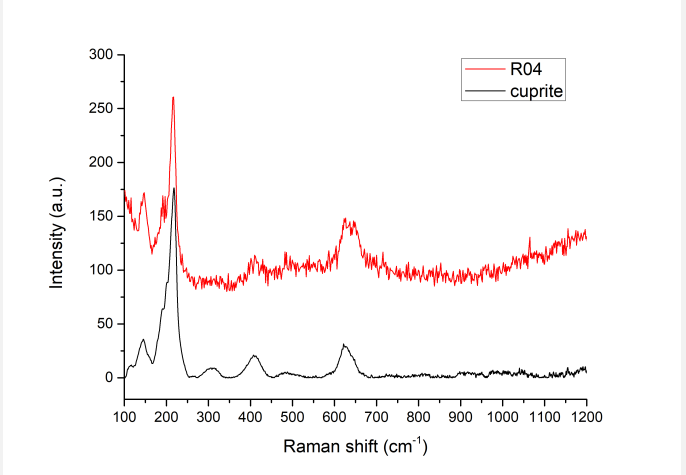

Fig. 15: Raman spectrum of point R04 performed on the red areas in CP4, as shown in Fig. 13, together with the reference for RRUFFID=R140763,

Credit LMC-CNRS, V.Valbi.

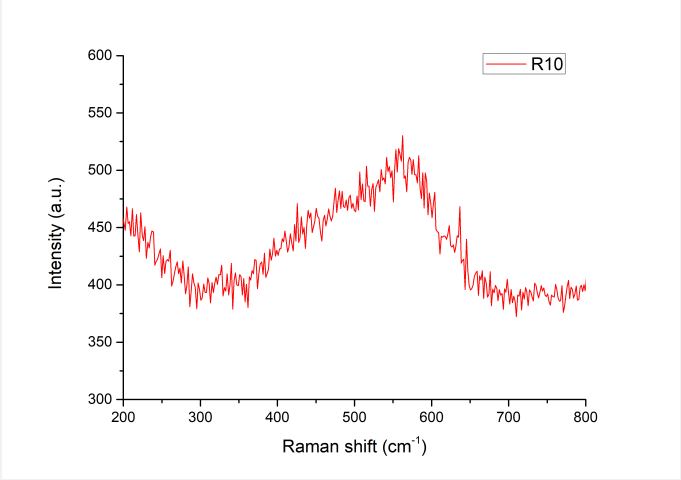

Credit LMC-CNRS, V.Valbi.

Fig. 16: Raman spectrum of point R10 performed on the blue CP4, as shown in Fig. 13, and identified as nano-cassiterite by comparison with the work of Ospitali et al. 2012,

Corrosion form	Uniform
Corrosion type	Unknown

Complementary information

None.

MiCorr stratigraphy(ies) – CS

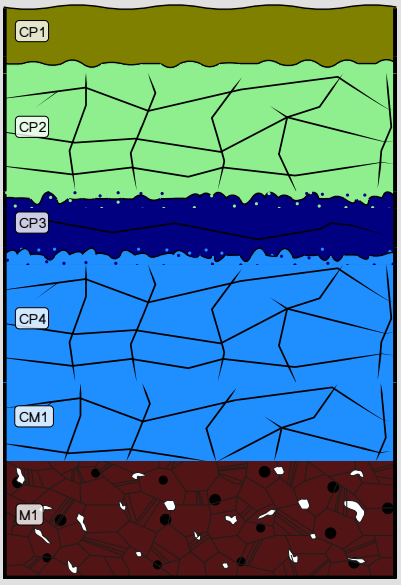

Fig. 17: Stratigraphic representation of the sample of the axe observed in cross-section under dark field using the MiCorr application. The characteristics of the strata are only accessible by clicking on the drawing that redirects you to the search tool by stratigraphy representation. This representation was build according to Fig. 9, Credit LMC-CNRS, V.Valbi.

Synthesis of the binocular / cross-section examination of the corrosion structure

The stratigraphies obtained by binocular and cross-section observation show a few differences. The blue, green and black CPs 1, 2 and 3 observed in binocular stratigraphy are not present in the cross-section stratigraphy. The location of sampling (Fig. 2) being different from the location of binocular observation can explain their absence in the sample taken. The CP4 observed under binocular microscope (Bi) probably could correspond to the olive green CP1 observed in cross-section (CS). CP5 observed under Bi could be the CP2 in CS. CP6 observed under Bi can correspond to the blue CP3 observed in CS. The light green CP7 under Bi shows a direct correspondence with the light blue CP4

identified in CS. The difference in the identified colours can be explained by the different perceptions of colours with the two observation modes and the operator bias. A CM was observed in CS, but was not documented in Bi.

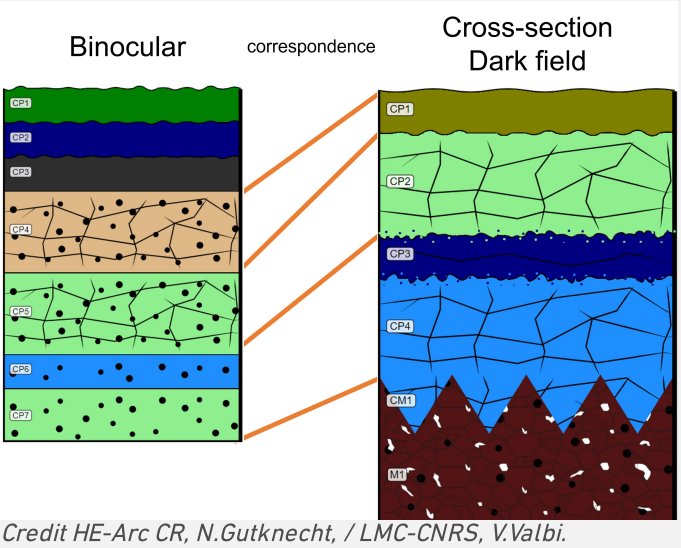

Credit HE-Arc CR, N.Gutknecht, / LMC-CNRS, V.Valbi.

Fig. 18: Stratigraphic representation side by side of binocular view and cross-section (dark field),

Conclusion

The winged axe has a low-tin bronze composition (8 mass% Sn) with sulfide inclusions that are typical of metallurgical processes of copper smelting from chalcopyrite-based minerals (Artemyev et al. 2019, Addis et al. 2015, Artioli et al. 2015). The metal microstructure revealed that the object underwent cold-working and annealing (final step). The metallography of this artefact can be compared to similar artefacts previously studied by Gabillot et al. 2021.

The corrosion products show the common decuprification phenomenon with associated tin enrichment leading to the formation of tin oxides and oxy-hydroxides such as cassiterite for CP4 (Robbiola et al. 1998, Ospitali et al. 2012) and mushistonite for CP2. Cuprite islets were also identified inside the cassiterite CP4 stratum, close to the interface with the metal, as well as S-rich inclusions identified as covellite (CuS). These sulfide inclusions in the CP are probably caused by the presence of sulfide inclusions in the original metal and do not come from the surrounding environment. Hydroxi-carbonates such as malachite and azurite are identified as well in the corrosion structure.

Documentation of this object was initiated because it suffers from a particular flaking corrosion. A possible explanation for this phenomenon might be the specific morphology of the corrosion strata, which appear powdery under binocular observation and strongly cracked and porous under cross-section observation. This results in poor adhesion of the corrosion strata and the flaking. Comparison with other objects with similar conservation problems may give new insight into this problem.

References

References on analytical methods and interpretation

1. Lafuente, B., Downs, R. T., Yang, H., Stone, N. (2015) The power of databases: the RRUFF project. In: Highlights in Mineralogical Crystallography, T. Armbruster and R. M. Danisi, eds. Berlin, Germany, W. De Gruyter, 1-30.
2. Ospitali, F., Chiavari, C., Martini, C., Bernardi, E., Passarini, F., Robbiola, L. (2012) The characterization of Sn-based corrosion products in ancient bronzes: a Raman approach. Journal of Raman Spectrpscopy, 43 (11), 1596-1603.
3. Robbiola L., Blengino M., Fiaud C., (1998) Morphology and mechanisms of formation of natural patinas on archaeological Cu–Sn alloys. Corrosion Science, 40 (12), 2083-2111.
4. Scott, D. (2006) Metallography and microstructure of ancient and historic metals. J Paul Getty Museum Publications.
5. Artemyev D. A., and Maksim N. A. (2019). Trace Elements of Cu-(Fe)-Sulfide Inclusions in Bronze Age Copper Slags from South Urals and Kazakhstan: Ore Sources and Alloying Additions. Minerals 9, no. 12: 746.

6. Addis, A.; Angelini, I.; Nimis, P.; Artioli, G. Late Bronze Age copper smelting slags from Luserna (Trentino, Italy): Interpretation of the Metallurgical Process. Archaeometry 2015, 58, 96–114.
7. Artioli, G.; Angelini, I.; Tecchiati, U.; Pedrotti, A. Eneolithic copper smelting slags in the Eastern Alps: Local patterns of metallurgical exploitation in the Copper Age. J. Archaeol. Sci. 2015, 63, 78–83.
8. Gabillot M. Métallurgistes en France orientale au Bronze moyen. Nouvelles analyses physico-chimiques et morphométriques, 2021.